Nanoscale

Accepted Manuscript

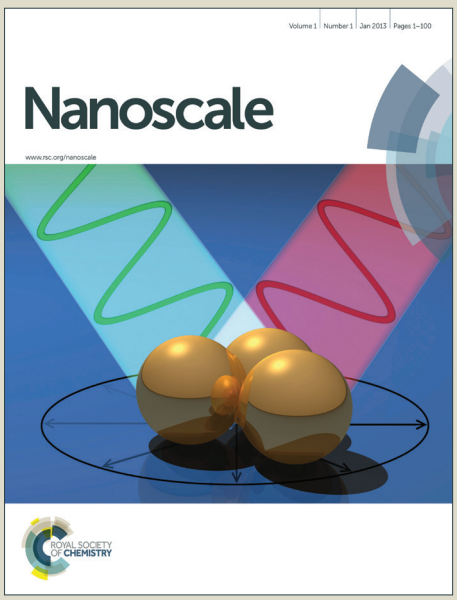

ROYAL SOCIETY OF CHEMISTRY

www.rsc.org/nanoscale

Journal Name

ARTICLE

A-site-deficiency facilitated *in situ* growth of bimetallic Ni-Fe nano-alloy: a novel coking-tolerant fuel cells anode catalyst

Received 00th January 20xx,
Accepted 00th January 20xx

DOI: 10.1039/x0xx00000x

www.rsc.org/

Yi-Fei Sun,[a] Jian-Hui Li,[b,*] Lin Cui,[a] Bin Hua,[a,c] Shao-Hua Cui,[d] Jian Li[c] and Jing-Li Luo[a,*]

To date, most investigations of Ni-Fe bimetallic catalysts for solid oxide fuel cells (SOFCs) have focused on materials with micro-scale particle sizes, which severely restrict their catalytic activity. In this study, we fabricated a Ni- and/or Fe- doped A-site-deficient $LaSrCrO_3$ perovskite (A-LSC) bimetallic anode material on which the *in situ* exsolution of uniformly dispersed nano Ni, Fe and Ni-Fe alloy with an average particle size of 25 to 30 nm was facilited by the introduction of A-site deficiency under a reducing atmosphere. The dopants were shown to significantly enhance the electrical conductivity of the material by many orders of magnitude. Further characterizations of the bimetallic material showed that the addition of Fe changed the reduction behavior and increased the amount of oxygen vacancies in the material. Fuel cell performance tests demonstrated that the prepared bimetallic anode catalyst with highly catalytically active nano Ni-Fe alloy promoted the electrochemical performance in 5000 ppm H_2S-syngas and improved the carbon deposition resistance compared to a monometallic anode catalyst.

Introduction

Main Solid oxide fuel cells (SOFCs) are a type of promising energy device that directly converts chemical energy in fuels into electricity [1]. Theoretically, SOFCs could operate on any combustible fuel, including H_2 [2, 3], syngas [4-6] and hydrocarbons [7, 8].

Much attention has been paid to the development of advanced and durable anode catalysts for SOFCs. The fundamental requirements for anode materials have been discussed and defined in previous research [1]. For example, these materials must have an adequate ionic and electronic conductivity, high mechanical strength, and catalytic activity for fuel oxidation. The Ni/yttria-stablized zirconia (Ni/YSZ) anode has been widely studied and has a good electrical conductivity and a high catalytic activity [9]. However, its long-term stability and redox stability are still challenging due to the coarsening of its Ni phase and the volume change that occurs during redox cycling. However, Ni/YSZ cermets also degrade due to their weak resistance to carbon deposition [10] and sulfur poisoning [11].

The addition of a second metal (i.e., guest) as a promoter has been effectively used to optimize the properties of the monometallic Ni-based anode catalyst [12-14], which can tune the material's catalytic performance by altering and modifying the electronic or structural parameters of the host metal [15]. Usually, some host and guest metals can form bimetallic alloys that have special synergetic effects or a bi-functional effect [16-19]. Among the various metal promoters, iron has been widely studied due to its easy accessibility and its effective enhancement to catalytic performance. Pasciak [20], Ishihara [21] and Lu [22] investigated Ni-Fe bimetallic composites with a Ni:Fe mol ratio of 3:1, 9:1 and 7:3, respectively, and found that the prepared anodes all exhibited better performance than a monometallic Ni-based cermet anode. In addition, an appropriate amount of iron added to the Ni-based anode has also been shown to enhance the tolerance of the cell to carbon deposition. Using a 10% additive Fe in a Ni+GDC anode significantly enhances the stability of the cell to reach 50 h of operation without degradation compared to the same anode without Fe, which shows a significant potential drop to 12 hours of operation under the same condition [23]. Gao et al. [24] also found that Ni-Fe-$La_{0.8}Sr_{0.2}Ga_{0.8}Mg_{0.115}Co_{0.085}O_3$ (Ni-Fe-LSGMCo) anodes showed good activity and stability for dimethyl ether (DME) oxidation without significant coke deposition. In-depth investigations performed by Fiuza et al. [25] showed that the Fe-Ni alloy/YSZ-GDC anode exhibited a desirable tolerance to carbon deposition by suppressing the formation of carbon.

Many other investigations have also shown that the preparation method for the Ni-Fe bimetallic anode catalyst also has a critical influence on the electrochemical performance and carbon resistance of these materials [22,23]. The traditional methods used to synthesize Ni-Fe bimetallic catalysts include a physical mixing method, the Pechi

[a] Department of Chemical and Materials Engineering, University of Alberta, Alberta, Canada, T6G 2V4. E-mail: jingli.luo@ualberta.ca.
[b] National Engineering Laboratory for Green Chemical Productions of Alcohols-Ethers-Esters, College of Chemistry and Chemical Engineering, Xiamen University, Xiamen, China, 361005. E-mail: jhli@xmu.edu.cn.
[c] School of Materials Science and Engineering, State Key Laboratory of Material Processing and Die & Mould Technology, Huazhong University of Science and Technology, Wuhan, China, 430074.
[d] General Equipment Department, China Petroleum Technology & Development Corporation, Beijing, China, 100028.

method and the glycine nitrite process (GNP) [25] and are typically low cost and simple processes. However, these methods can only fabricate catalysts with uneven dispersions and larger particle sizes, which limit the surface area and restrict the number of active sites. The impregnation method is another type of widely used methods for depositing a Ni-Fe alloy catalyst onto a support matrix [26]. However, this process is time-consuming and not well controlled, which also leads to a weak distribution of the loading infiltrated phase.

Recently, an *in situ* fabrication strategy has been developed and used to prepare perovskite oxide with the addition of uniformly distributed nano metallic particles. In this process, diverse reducible elements could be doped into the B sites of perovskite and also be partly exsolved out of the lattice *in situ* under a reducing atmosphere. It is reported that this method has been successfully used to synthesize $La_{0.52}Sr_{0.28}Ni_{0.06}Ti_{0.94}O_3$ perovskite oxides [27] and Fe- and Ni-doped $La_{0.2}Sr_{0.25}Ca_{0.45}TiO_3$ (LSCT) perovskite [28], which all utilized the *in-situ* exsolution of large amounts of nano particles on the surface of the perovskite oxide. It was also shown that this exsolution phenomenon could be effectively altered by the introduction of A-site deficiencies in perovskite, which can be regarded as one of the driving forces for the reduction of B-site metals. Previous work performed by our group has shown that Ni could preferably exsolve onto an A-site-deficient lanthanum strontium chromite (LSC) perovskite, and the functional materials exhibited a desirable electrochemical performance in both sweet and sour fuels. Therefore, the approach should be a promising and effective way to fabricate Ni-Fe alloy particles on perovskite parents.

Consequently, in this study, the Ni- and Fe-doped A-site-deficient LSC perovskite anode catalyst was synthesized, and the electrochemical performance of the material using different fuels was also evaluated. The characteristics of the Ni-Fe bimetallic catalysts are investigated in detail to elucidate the synergetic effect between Ni and Fe in the nano alloy.

Experimental

Fabrication of electrode materials.

The glycine nitrate combustion method was used to fabricate the Ni- and/or Fe-doped Lanthanum strontium chromite anode materials, which are denoted as LSCNi, LSCFe and LSCNi-Fe, respectively. The Ni, Fe or Ni-Fe (mol ratio of Ni:Fe = 3:1) dopant contents in the total B-site cations were equal to 15 mol%. Certain amounts of $La(NO_3)_2{\cdot}6H_2O$, $Sr(NO_3)_2$, $Ni(NO_3)_2{\cdot}6H_2O$, $Fe(NO_3)_3{\cdot}9H_2O$, $Cr(NO_3)_3{\cdot}9H_2O$ and glycine were first dissolved in deionized water. The molar ratio of glycine to the total content of the metal cations was 2:1. The solution was stirred thoroughly and then heated on a hot plate at 500°C until self-combustion occurred. The powders were ground and further calcined at 1100°C for 3 h to generate different anode materials. The designations of each material are shown in Table 1.

Table 1. Designation of various materials.

Abbreviation	Anode compositions
LSCNi	$(La_{0.7}Sr_{0.3})(Cr_{0.85}Ni_{0.15})O_{3-x}$
LSCFe	$(La_{0.7}Sr_{0.3})(Cr_{0.85}Fe_{0.15})O_{3-x}$
LSCNi-Fe	$(La_{0.7}Sr_{0.3})(Cr_{0.85}Ni_{0.12}Fe_{0.03})O_{3-x}$

Fuel cell fabrication

Fuel cells were fabricated using commercial YSZ disks (FCM, "fuelcellmaterials.com") as electrolytes with a thickness of 100 μm and a diameter of 25 mm. The cathode used was a mixture of equal weights of YSZ powder (TOSHO Company) and strontium-doped lanthanum manganese (LSM). The anode used was prepared by mixing equal weights of YSZ and the anode materials. Both the cathode and anode inks were prepared using oxide powders dispersed in terpineol mixed with 10% polyethylene glycol (PEG) as a screen-printing binder. The electrode inks were deposited onto the YSZ electrolyte disc using screen printing to form a membrane electrode assembly (MEA) with a circular diameter of 1 cm^2; then, the cell was sintered at 1100°C for 2 h to form a good combination between the electrodes and the electrolyte. The platinum and gold pastes were painted onto the cathode side and anode side, respectively, to serve as the current collectors.

Single cell tests were performed in a vertical furnace in a coaxial two-tube (i.e., inlet and outlet) setup. The outer tube (i.e., the outlet) was sealed (Ceramabond 503, Aremco Products) directly to the outer edge of the anode side of the single-cell electrolyte to avoid the leakage of fuel gas. A Thermolyne F79300 tubular furnace was used to heat the cell setup. Syngas mixed with 5000 ppm H_2S (5000 ppm H_2S in syngas (60% CO balance by 40% H_2) and 5000 ppm H_2S-H_2 (Praxair)) were used as the fuel at a rate of 75 mL min^{-1}. The electrochemical performance of the fuel cell reactor was measured using a Solartron 1287 instrument with a 1255 frequencer. The polarization resistance of the cell was measured using electrochemical impedance spectroscopy (EIS) in the frequency range from 1 MHz to 0.1 Hz at open circuit voltage (OCV). All data were analyzed using the Z-View and C-View softwares.

Materials characterization

The phase structures of the synthesized powders were identified using a Rigaku Rotaflex X-ray diffractometer (XRD) with Cu Ka radiation, and the data were analyzed using JADE 5.0 software.

The micromorphology of the materials was determined by a JEOL 6301F scanning electron microscope (SEM). Additional information was gathered using an EOL JEM2100 transmission electron microscope (TEM) with an energy-dispersive X-ray spectroscopy (EDS) detector. The reduced samples for SEM or TEM analysis were exposed to a dry 5% H_2/N_2 atmosphere at a temperature of 800°C for 4 h.

Thermogravimetric analysis (TGA) measurements were conducted using a TA Instruments SDT Q600 under 5% H_2/N_2

from 100°C to 900°C with a flow rate of 20 mL min^{-1} and a heating rate of 20 °C min^{-1}.

Hydrogen temperature programmed reduction (H_2-TPR) was performed using an AutoChem II 2920 instrument (Micromeritics, USA) equipped with a thermal conductivity detector (TCD). All samples were treated with helium at 1000°C for 30 min before H_2-TPR. The flow rate for this analysis was 10% H_2/Ar at 10 mL min^{-1}, and the temperature ramping rate was 10°C min^{-1}.

Thermal expansion coefficients (TECs) were measured using rectangular bar samples (5 mm x 5 mm x 20 mm) from room temperature to 900°C at a heating rate of 5°C min^{-1} using a dilatometer instrument (NETZSCH).

The temperature-programmed oxidation (TPO) method was used to characterize and quantify the carbon deposition on the anode materials after various treatments. The samples were placed in an alumina tube, loaded into the TPO apparatus and exposed to a flow of 10% O_2 balanced with He at 50 mL min^{-1} for 1 h. The temperature was then increased from room temperature to 900°C at 20°C min^{-1}, and the effluents were analyzed by the mass spectrometer (Thermo star 301). Signals for m/z = 44 (CO_2), m/z = 28 (CO only; the residual N_2 contribution and CO_2 contribution to 28 were removed from analysis), m/z = 32 (O_2) and m/z = 18 (H_2O) were monitored during the TPO experiments. Prior to the TPO analysis, the mass spectrometer signals had been calibrated using gas mixtures of known concentrations.

The Van der Pauw four points method was used to measure the electrical conductivity of the synthesized samples using ProbStat instruments in air.

Results

The XRD patterns for the fresh anode materials are shown in Figure 1(a). It is clearly shown that both the monometallic dopant and bimetallic dopants have no influence on the chemical structure of the material. Additionally, all materials exhibit a perovskite structure without impurities. The XRD profiles of all reduced materials are shown in Figure 1 (b), and the materials are denoted as R-LSCNi, R-LSCFe and R-LSCNi-Fe. It is shown that after the reduction in 5% H_2/N_2 at 800°C for 4 h, a metallic Fe phase was detected for R-LSCFe only as indexed in the figure. For the R-LSCNi sample, a diffraction peak that can be attributed to metallic Ni was observed in the XRD profile. It is known that Fe and Ni are adjacent to each other in the periodic table; thus, they can easily form a solid solution phase with various ratios. For the R-LSCNi-Fe sample with Ni:Fe=3:1, a solid solution of Awaruite $FeNi_3$ (JCPDS38-0419) was found in the structure. Combined with the XRD patterns for LSCNi and LSCFe, it can be inferred that the metallic Fe and Ni may firstly form on the LSCNi-Fe sample and then generate the alloy.

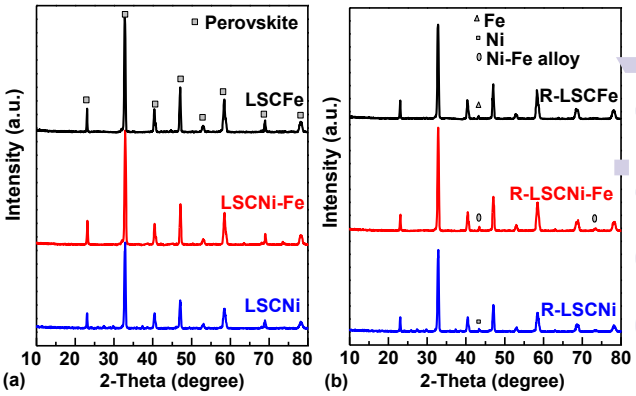

Figure 1. XRD patterns for (a) fresh anode materials and (b) reduced anode materials. All materials were reduced in 5% H_2/N_2 at 800°C for 4 h.

The reducibility of Fe and Ni in each perovskite oxide and the synergistic effect between Fe and Ni were characterized using H_2-TPR technology, and the corresponding results are plotted in Figure 2. The curve of LSCNi exhibits two H_2 consumption peaks at ~520°C and 620°C. It has been previously reported that the reduction behavior of Ni consists of two stages including an α-peak at a lower temperature (~500°C) due to the reduction of Ni^{3+} into Ni^{2+}, and a β-peak at a higher temperature (~600°C) that is associated with the reduction of Ni^{2+} into metallic Ni [29, 30]. For Fe-doped perovskite, the reduction profile for the LSCFe sample show three groups of multiple peaks from 400°C to 600°C, which can be attributed to the reduction of Fe^{3+} to Fe^{2+}, Fe^{2+} to Fe^0 and Fe^{3+} to Fe^0 respectively [31]. With the addition of Fe to Ni, the Ni-Fe bimetallic material only exhibits one H_2 consumption peak at ~500°C. This phenomenon indicates that the formation of the Ni-Fe composite significantly changes the reduction behavior of the Ni and Fe oxides, and the two different metals were reduced simultaneously, which should be regarded as evidence for the formation of the alloy for the bimetallic catalysts [32, 33].

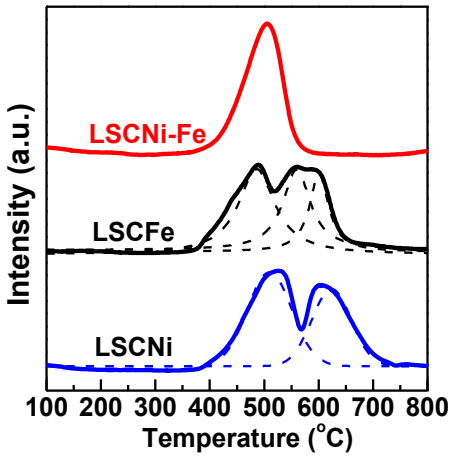

Figure 2. H_2-TPR profiles for different anode materials.

Theoretically, based on the Ni-Fe phase diagram in Figure 3 [34], at least one regular alloy with the composition of Ni_3Fe could formed at this experiment condition. However, at same condition, the alloys with the composition of NiFe and Ni_3Fe_2 and Ni_2Fe have also been reported [35-37]. Previous report has demonstrated that a significant fraction of iron on supported catalysts could be alloyed with nickel simply after treatment of H_2 [38]. Consequently, it can be inferred that the formation of alloy under this experiment condition is favorable.

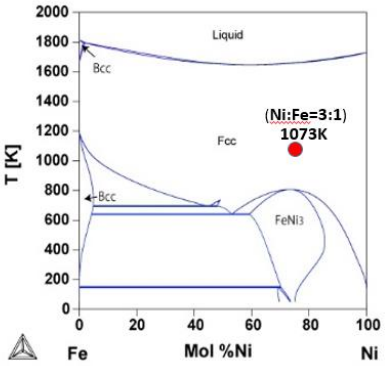

Figure 3. Phase diagram of bimetallic Ni-Fe system[34].

The TGA measurements for the different samples were conducted in 5% H_2/N_2 from 100°C to 900°C, and the corresponding curves are shown in Figure 4. The weight loss is primarily due to the formation of oxygen vacancies, namely the reduction of metal oxide and escape of oxygen ion. The LSCNi sample started to lose weight at 515°C and showed a total weight loss of ~2.5%. The results of the LSCFe material show that its weight loss began at ~400°C and exhibited a total loss weight percentage of 2%. In comparison, the formation process of oxygen vacancies from the lattice of LSCNi-Fe started at a temperature similar to that of LSCFe. However, the total weight loss percentage is close to 3%, which is significantly higher than that of LSCFe and LSCNi. These results indicate that the formation of an alloy facilitates the formation of oxygen vacancies and further benefits the exsolution of both Ni and Fe. Inaddition, it can be gained that the non-stoichiometry of oxygen ion is 0.42. The exsolution of Ni and Fe in the material should have the same reaction rate. So, it can be calculated that 22.3% of Fe and 25% of Ni could be exsolved to form nano particles, respectively, for the LSCNi-Fe samples. And 77.7% of Fe and 75% of Ni are still in the oxidized state.

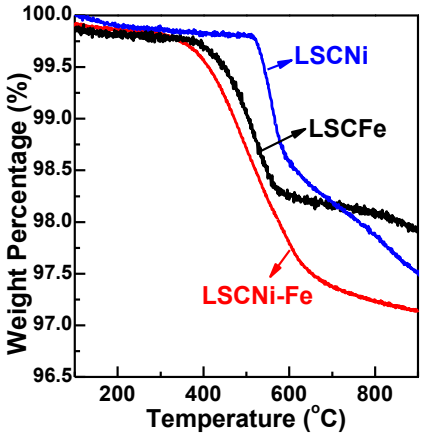

Figure 4. TGA curves of the fresh LSCNi, LSCFe and LSCNi-Fe samples measured in 5% H_2/N_2.

During SOFC operation, the cell experiences high temperatures for a prolonged period of time. Consequently, the thermal expansion coefficient (TECs) of the electrode and the electrolyte should be similar to generate lowest possible thermal stress in the SOFC stacks. To determine the mechanical compatibility of the fabricated bimetallic perovskite anodes with the YSZ electrolyte used in fuel cell, a thermal expansion measurement was performed in air. Figure 5 shows the TECs for the fabricated anode and the YSZ electrolyte from 400 K to 1200 K. The TEC of the YSZ electrolyte is shown to be ~11×10^{-6} K^{-1} throughout the temperature range regardless of the oxygen partial pressure, the LSCNi-Fe is shown to have a TEC of ~10.7×10^{-6} K^{-1}, which is similar to that of the YSZ, indicating that the LSCNi-Fe anode is a suitable candidate for use as an SOFC electrode.

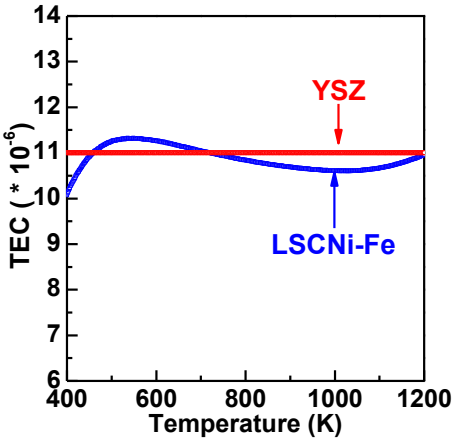

Figure 5. TECs of LSCNi-Fe and YSZ materials in air from 400 K to 1200 K.

The electrical conductivities of the pre-reduced materials in air are shown in Figure 6(a) as a function of temperature. For comparison, data for LSC without any substitutions are also included in Figure 6. In each test, the measurement was conducted for 30 minutes to reach equilibrium. Additionally,

expected, all samples exhibited a linear metallic conductivity behavior, suggesting that the electrical conductivity behavior is a thermally activated process that obeys the small polaron conductivity mechanism expressed by the equation shown below:

$$\sigma = (A / T) \exp(-Ea / KT) \quad (1)$$

where A is a pre-exponential factor, K is the Boltzmann's constant, T is the absolute temperature, and E_a is the reaction activation energy.

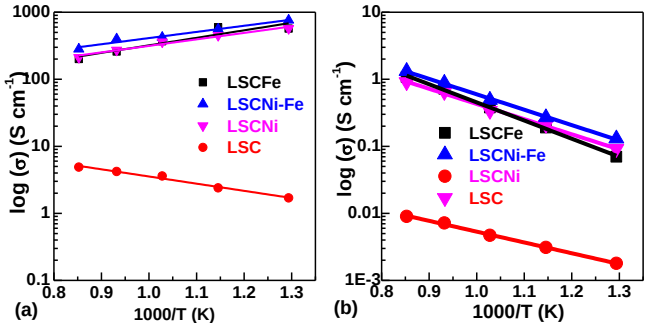

Figure 6. Electrical conductivities of various materials in: (a) air and (b) 5%H_2/N_2 as a function of temperature.

It can be found in Figure 6(a) that the conductivity increases with the temperature increases for LSC. And all doped materials show descending trend of the conductivity as the temperature increase. The enhanced electrical conductivity of all doped materials can be simply explained by the charge compensation phenomenon (e.g., Cr^{3+} to Cr^{4+}) after the substitution of low valence metals (e.g., Ni^{2+} and Fe^{2+}) for Cr^{3+}, which facilitates the transportation of electrons. It is also shown that the LSCNi-Fe material shows a higher conductivity at higher temperatures compared to LSCNi and LSCFe. A similar phenomenon has been reported with Co- and Ni-Co-doped $La_{0.85}Sr_{0.15}CrO_3$ perovskite [39]. It is postulated that the higher conductivity is related to the interaction between the Ni and Fe ions with higher mobilities at elevated temperature.

Fig. 6 (b) shows the dependence of electrical conductivity with temperature in 5%H_2-N_2. As what can be observed in Figure 6(b), the conductivity increased as the temperature increased for all materials. And this value was obviously improved for the doped compositions. The LSCNi-Fe anode exhibits the electrical conductivity of around 1.2 S cm^{-1} at 800 ^oC, which is comparable to the result of excellent perovskite anode $La_{0.75}Sr_{0.25}Cr_{0.5}Mn_{0.5}O_3$ (LSCM) of 0.96 S cm^{-1} [40], indicating that the LSCNi-Fe could provide sufficient electron transfer paths for the reaction.

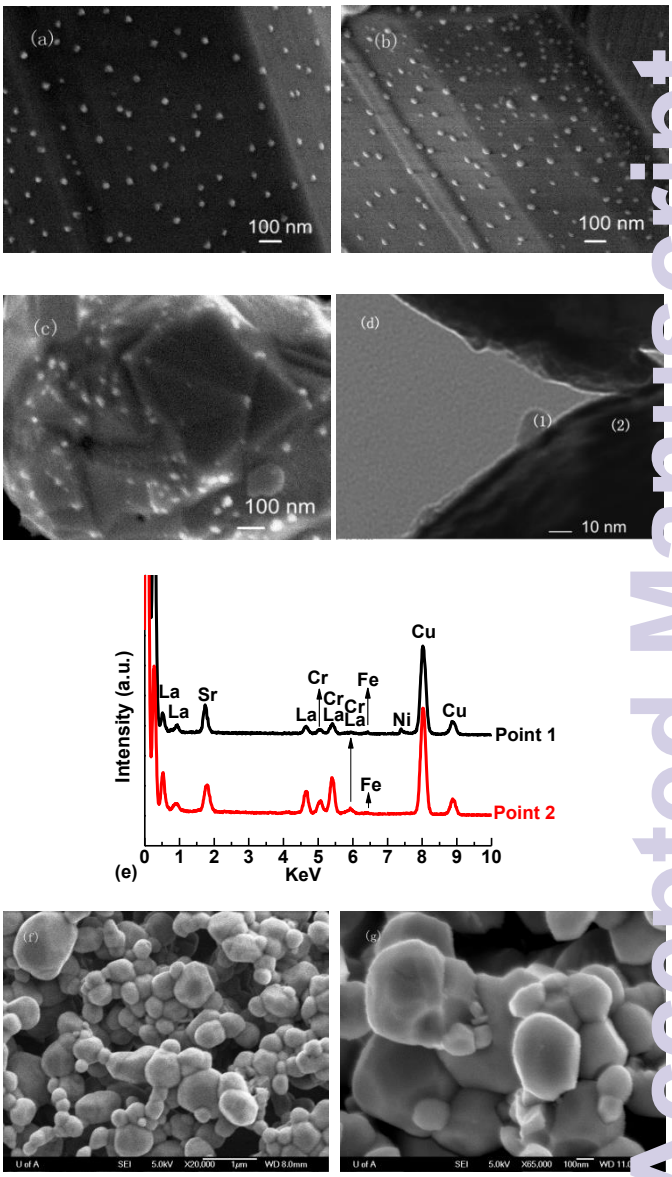

Figure 7. SEM images for the (a) LSCNi (b) LSCFe and (c) LSCNi-Fe materials reduced at 800^{o}C for 4 h; (d) TEM micrograph of the exsolved nano-particle anchored to the bulk LSCNi-Fe material; (e) EDX analysis for points 1 and 2 on the TEM image shown in (d). (f) and (g) are the SEM images for the LSCFe materials reduced at 800 ^{o}C for 4 h and LSCNi-Fe material before reduction, respectively.

The SEM images of the reduced LSCNi, LSCFe and LSCNi-Fe samples are shown in Figure 7 (a), (b) and (c), respectively. All samples have been pre-treated in 5% H_2-N_2 at 800^{o}C for 4 h. It is shown that all reduced samples show well-distributed nano particles covering the surface of the perovskite matrix. The average diameter of the particles is ~25 to 30 nm. In comparison, Figure 7(f) and (g) exhibit the SEM images for LSCFe materials reduced at 800 ^{o}C for 4h and LSCNi-Fe material before reduction. Clearly, no exsolution of any metallic nano particles could be found on the surface the materials. Inaddition, it has been observed that the exsolved nano

particle will grow as the reaction goes under anode operating condition.

The TEM image for the LSCNi-Fe sample is shown in Figure 7 (d). The exsolution of the nano alloy particles with diameters of ~25 nm are shown at the edge of the perovskite parent. The presence and distribution of Ni and Fe within one individual alloy particle were further verified using the TEM-EDS spectrum. As shown in Figure 7 (e), the chemical composition of the bulk material (point 2) was significantly different from the nano particle (point 1), where the significant peaks can be attributed to Ni and Fe, indicating the presence of the Ni-Fe alloy. In comparison, the intensities of the peaks for Fe and Ni are relatively weak. The SEM and TEM results thus agree with the XRD and H_2-TPR results, which indicate the presence of the Ni-Fe alloy.

The detailed I-V and power density curves for the fuel cells with different anodes operating in 5000 ppm H_2S-H_2 are shown in Figure 8(a). The maximum power density (MPD) of a fuel cell with an LSCNi anode and an LSCFe anode were 460 mW cm^{-2} with a maximum current density (MCD) of ~1300 mA cm^{-2}, and 360 mW cm^{-2} with an MCD of ~1000 mA cm^{-2}, respectively. In comparison, a fuel cell with a LSCNi-Fe bimetallic anode could generate an MPD of 560 mW cm^{-2} with an MCD of ~1700 mA cm^{-2}. These results imply that all of the tested anode catalysts have sufficient catalytic activities for the oxidation of hydrogen.

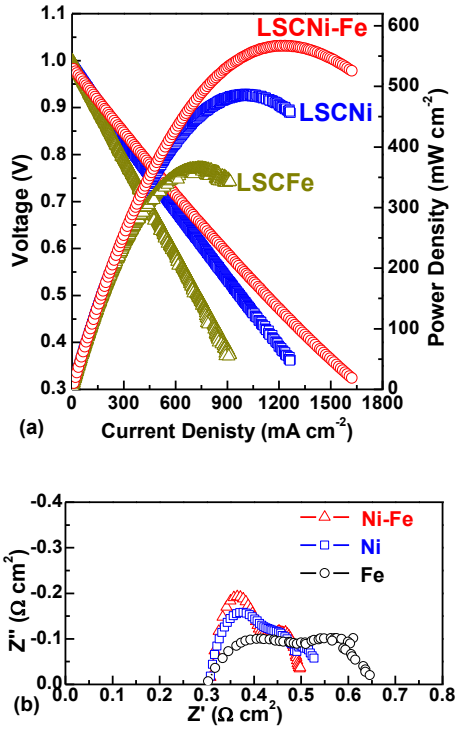

Figure 8. (a) Current density vs. voltage and power density curves, and (b) electrochemical impedance spectra for fuel cells with LSCNi, LSCFe and LSCNi-Fe anodes using 5000 ppm H_2S-H_2 fuel at 800°C.

To create a clear comparison of the electrochemical performances of the various cells tested, the electrochemical impedance spectra (EIS) of the cells fueled with 5000 ppm H_2 H_2 at 800°C under OCV conditions were also measured and are shown in Figure 8(b). At the same reaction temperature, the electrolyte resistance of each cell was ~0.3 Ω cm^2. The activation polarization resistances of the LSCNi, LSCFe and LSCNi-Fe fuel cells were 0.35, 0.25 and 0.2 Ω cm^2, respectively, indicating that the addition of Fe to Ni decreases the activation polarization resistance of the anode, which is likely the primary reason for the observed improved electrochemical performance.

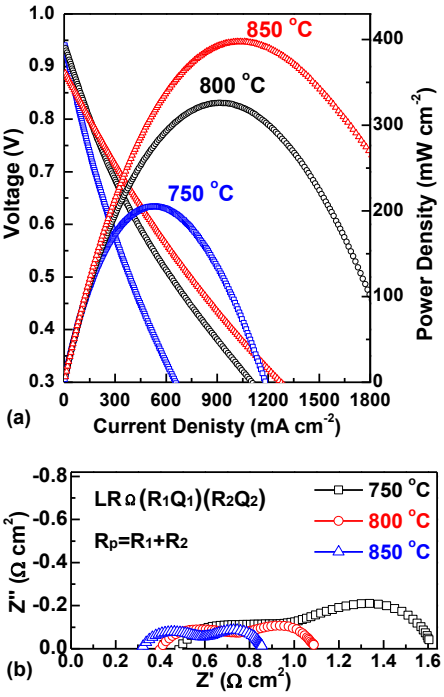

Figure 9. (a) Current density vs. voltage and power density curves, and (b) electrochemical impedance spectra for fuel cells with an LSCNi-Fe anode using 5000 ppm H_2S-syngas fuel at different temperatures.

The electrochemical performances of LSCNi-Fe fuel cells fed with 5000 ppm H_2S-syngas are demonstrated by the I-V and power density curves shown in Fig. 9 (a). The OCV values at each temperature are similar to their theoretical values. As the reaction temperature rose from 750°C to 850°C, the MPD output and MCD values increased from 210 to 400 mW cm^{-2} and from 680 mA cm^{-2} to 1300 mA cm^{-2}, respectively. These results demonstrate that the LSCNi-Fe anode has good activity to catalyze the oxidation reaction of syngas.

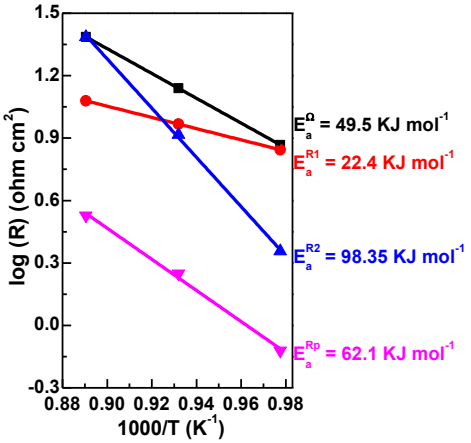

Figure 10. Electrochemical impedance spectra of a fuel cell with an LSCNi-Fe anode measured in 5000 ppm H_2S-syngas between 750 °C and 850 °C under open-circuit conditions. Arrhenius plot of the resistances measured at different temperatures.

The impedance data of a single cell with an LSCNi-Fe anode measured under OCV conditions between 750 to 850°C are given in Figure 9 (b). The best fitting results to the equivalent circuit of $LR_{\Omega}(R_1Q_1)(R_2Q_2)$ for all EIS have been obtained, where R_{Ω} represents the pure Ohmic resistance. Each of the parallel circuits with resistance Ri and constant phase element Qi accounts for the respective depressed semicircle going from high to low frequencies. A parasitic inductance L was added to consider the contribution of the equipment. This fitting result indicates that two different electrodes processed corresponding to the high- and low-frequency arcs control the electrochemical reaction. The total polarization resistance of the cell (R_p) can be expressed by the sum of R_1 and R_2. The fitted impedance parameters of the cell at different temperatures under OCV conditions are plotted in Figure 10. The apparent activation energies of the polarization resistances in the low and high frequency ranges and the total polarization resistance were calculated to be 22.4, 98.6 and 62.1 KJ mol^{-1}, respectively. The apparent activation energy of the Ohmic resistance was found to be 49.5 KJ mol^{-1}. These activation energy results further show that the increase in cell performance was primarily due to the electrochemical kinetics of the electrode.

In addition to the catalytic activity, the resistance to carbon deposition is another important parameter for the evaluation of the functional anode materials used in hydrocarbon fuels. Previous studies have claimed that Ni is prone to carbon deposition, and Fe has a better tolerance to coking [19]. Figure 11 shows the O_2-TPO profiles of various fresh materials after treatment with syngas for 24 h at 850°C.

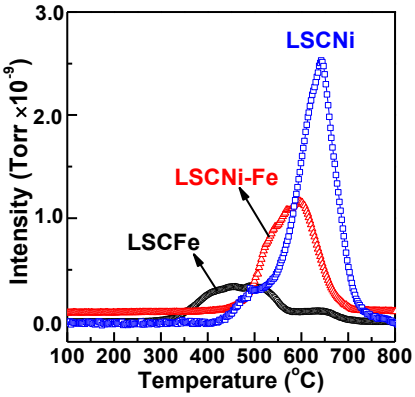

Figure 11. TPO curves of various materials treated with syngas in 850 °C for 24 h.

The CO_2 peak areas were 3.1*10^{-7}, 1.63*10^{-7}, and 6.1*10^{-9} fo LSCNi, LSCNi-Fe and LSCFe, respectively. Based on these results, it can be concluded that the addition of Fe effecti suppresses the formation of carbon deposition on th material. However, it also can be found by comparing the curves that the peak position of the CO_2 of the material shifts from 650°C to ~590°C when Fe is added to LSCNi. For LSCFe, the location of the primary peak is ~450°C. Based on previous studies of the density functional theory (DFT) calculation, a bi metallic alloy can preferentially remove carbon deposition on the surface of the electro-catalyst rather than facilitate t formation of carbon-carbon bonds, as monometallic Ni doe [18, 41]. This conclusion is consistent with our experimenta results, which show that the introduction of Fe significantly facilitates the removal of carbon deposition.

Discussion

The A-site-deficient LSC perovskite with co-doping of Ni and Fe was successfully fabricated, and the phenomenon of *in sit* exsolution of the nano Ni-Fe alloy was detected at SO operating conditions. The bimetallic anode has been identified as catalytically active in sour gas and significantly more carbon tolerant than monometallic Ni anodes. The XRD patterns fo fresh samples show that after sintering, all dopants have dissolved into the perovskite lattice, and no impurities are present in the fresh samples. The *in situ* treatment of th reducing atmosphere on the samples forces the reducible ions (e.g., Fe and Ni) to exsolve out of the lattice to form metall nano particles. This process has been identified by the XRD results for the reduced samples.

Compared to a monometallic catalyst, the LSCNi-Fe sample showed multiple steps of the reduction process. It postulated that in the first step, the Ni^{2+} and Fe^{3+} or Fe^{2+} are synchronously reduced to form Ni and Fe, anchored to th surface of the perovskite, respectively. Based on the description in the experimental procedures, the stoichiometri ratio of Ni to Fe is 3:1. The phrase diagram shows that the formation of the Ni-Fe alloy with the ratio of 3:1 is thermodynamically favorable under these reduct

conditions. Consequently, it is reasonable to conclude that the exsolved Fe and Ni migrate to the surface at similar diffusion velocities to form the Ni-Fe alloy in the second step because they have approximately the same Tammann temperature. Thus, the aggregation of metallic Ni and metallic Fe occurs simultaneously during the process of alloy formation. However, the XRD results for the reduced samples did not show any significant diffraction peaks that could be attributed to Ni and Fe. In this case, these particles likely exist at sizes below the detection limitation of the XRD process.

The formation of the alloy has a significant influence on the reducibility of the Fe and Ni, which is shown in the results of the H_2-TPR and TGA analyses in the reducing atmosphere. Only one wide H_2 consumption peak from 380°C to 600°C is shown for the LSCNi-Fe sample, which could be attributed to the similar reduction behaviors of Ni and Fe. In comparison, the monometallic catalyst has reduction peaks only between 400°C and 700°C. The shift of the reduction peaks to lower temperatures indicates that the formation of the alloy facilitates the exsolution of Ni and Fe out of the lattice. Additionally, the results of the TGA analysis suggest the promotion effect on the reduction of metals, in which the temperature where the LSCNi-Fe began to lose weight is ~380°C. This value is consistent with the results in the TPR analysis and is lower than that of the monometallic catalysts. The bimetallic material shows a total weight loss of 3%, which is 20% and 33% higher than those of LSCNi and LSCFe, respectively, demonstrating that a larger amount of metal combined with more oxygen vacancies form during this process. Both of these two factors will benefit the electrochemical reaction and further enhance the catalytic performance of the material.

However, the co-doping of Ni and Fe in the LSC perovskite is shown to enhance the electrical conductivity of the material because charge compensation (e.g., Cr^{3+} to Cr^{4+}) occurs after the doping of low valence metals into B sites for partial substitution of Cr^{3+} to ensure charge neutralization within the materials and create more charge carriers. In addition, the exsolution of the metals contributes to electron transportation during the reaction. Consequently, the electrochemical performance tends to be improved.

Additionally, it is widely accepted that the formation of carbon deposition may block the pores and cover the reaction sites in the material, influencing the fuel diffusion and leading to a decrease in catalytic activity. The results of the calculation of the activation energy (E_a) for each polarization resistance behavior show that the rate-determining step of the reaction is the fuel diffusion (R_2) for the LSCNi-Fe and LSCNi materials, which have an E_a of 98.35 KJ mol^{-1} and 121.83 KJ mol^{-1}, respectively. The TPO results show that the LSCNi-Fe anode has a better carbon deposition tolerance than the LSCNi anode. The addition of Fe decreases the activation energy for fuel diffusion by suppressing the formation of carbon deposition. Consequently, the performance tends to be enhanced.

Conclusions

The Ni- and Fe-co-doped LSC bimetallic perovskite anode material with A-site deficiencies was successfully prepared by the glycine combustion method. The exsolution of the Ni-Fe nano alloy was detected on the *in situ* reduced samples using SEM and TEM. The TGA and H_2-TPR profiles showed that the addition of Fe helped create more oxygen vacancies and promoted the reducibility of the materials, respectively. The anode material with the exsolved Ni-Fe alloy showed a desirable electrical conductivity, electrochemical performance in sour H_2 and syngas, and better resistance to carbon deposition compared to a Ni monometallic anode.

Acknowledgements

This study was supported by the Natural Sciences and Engineering Research Council (NSERC) of the Canada Strategic Project Grant and the National Natural Science Foundation of China under grant 21303141.

References

[1] S. Jiang and S. Chan, *J. Mater. Sci.*, 2004, **39**, 4405-4439.

[2] V.B. Vert, F.V. Melo, L. Navarrete and J.M. Serra, *Appl. Catal. B: Environ.*, 2012, **115-116**, 346-356.

[3] J. Wan, J.H. Zhu and J.B. Goodenough, *Solid State Ionics*, 2006, **177**, 1211-1217.

[4] T.S. Li, M. Xu, C. Gao, B. Wang, X. Liu, B. Li and W.G. Wang, *J. Power Sources*, 2014, **258**, 1-4.

[5] Z. Xu, J. Luo and K.T. Chuang, *J. Electrochem. Soc.*, 2007, **154**, B523.

[6] A.I. Marquez, T.R. Ohrn, J.P. Trembly, D.C. Ingram and D.J. Bayless, *J. Power Sources*, 2007, **164**, 659-667.

[7] Z. Ding, X. Chen, M. Antonietti and X. Wang, *ChemSusChem*, 2011, **4**, 274-281.

[8] T. Horita, K. Yamaji, T. Kato, N. Sakai and H. Yokokawa, *J. Power Sources*, 2004, **131**, 299-303.

[9] W. Wang, C. Su, Y. Wu, R. Ran and Z. Shao, *Chem. Rev.*, 2013, **113**, 8104-8151.

[10] H. He and J.M. Hill, *Appl. Catal. A: Gen.* 2007, **317**, 284-292.

[11] J.W. Yun, S.P. Yoon, J. Han, S. Park, H.S. Kim and S.W. Nam, *J. Electrochem. Soc.*, 2010, **157**, B1825.

[12] A. Kitla, O.V. Safonova and K. Fottinger, *Catal. Lett.*, 2013, **143**, 517-530.

[13] V.M. Gonzalez-delaCruz, R. Pereñiguez, F. Ternero, J.P. Holgado and A. Caballero, *J. Phy. Chem. C*, 2012, **116**, 2919-2926.

[14] C.M. Grgicak, M.M. Pakulska, J.S. O'Brien and J.B. Giorgi, *J. Power Sources*, 2008, **183**, 26-33.

[15] F. Tao, *Chem. Soc. Rev.*, 2012, **41**, 7977-7979.

[16] Z.G. Lu, J.H. Zhu, Z.H. Bi and X.C. Lu, *J. Power Sources*, 2008, **180**, 172-175.

[17] A. Ringuedé, J.A. Labrincha and J.R. Frade, *Solid State Ionics*, 2001, **141–142**, 549-557.

[18] W. An, D. Gatewood, B. Dunlap and C.H. Turner, *J. Power Sources*, 2011, **196**, 4724-4728.

[19] B. Huang, S.R. Wang, R.Z. Liu and T.L. Wen, *J. Power Sources*, 2007, **167**, 288-294.

[20] C.J. Fu, S.H. Chan, X.M. Ge, Q.L. Liu and G. Pasciak, *Int. J. Hydrogen Energ.*, 2011, **36**, 13727-13734.

[21] Y.W. Ju, H. Eto, T. Inagaki, S. Ida and T. Ishihara, *J Power Sources*, 2010, **195**, 6294-6300.

[22] X.C. Lu, J.H. Zhu and Z.H. Bi, *Solid State Ionics*, 2009, **180**, 265-270.

[23] H. Kan and H. Lee, *Catal. Comm.*, 2010, **12**, 36-39.

[24] W. Shi-zhong and G. Jie, *Electrochem. Solid-State Lett.*, 2006, **9**, A395-A398.

[25] R. da Paz Fiuza, M. Aurélio da Silva and J.S. Boaventura, *In. J. Hydrogen Energ.*, 2010, **35**, 11216-11228.

[26] S.P. Jiang, *In. J. Hydrogen Energ.*, 2012, **37**, 449-470.

[27] D. Neagu, G. Tsekouras, D.N. Miller, H. Menard and J.T. Irvine, *Nat. chem.*, 2013, **5**, 916-923.

[28] A. Yaqub, N.K. Janjua, C. Savaniu and J.T.S. Irvine, *In. J. Hydrogen Energ.*, 2015, **40**, 760-766.

[29] A. Jahangiri, H. Aghabozorg and H. Pahlavanzadeh, *In. J. Hydrogen Energ.*, 2013, **38**, 10407-10416.

[30] K. Rida, M.A. Peña, E. Sastre and A. Martinez-Arias, *J. Rare Earths*, 2012, **30**, 210-216.

[31] W. Gao, C. Li, H. Chen, M. Wu, S. He, M. Wei, D.G. Evans and X. Duan, *Green Chem.*, 2014, **16**, 1560-1568.

[32] S. Bhatia, J. Beltramini and D.D. Do, *Catal. Today*, 1990, **7**, 309-438.

[33] B.D. McNicol, *J. Catal.*, 1997, **46**, 438-440.

[34] Y.F. Sun, J.H. Li, S.H. Cui, K.T. Chuang and J.L. Luo, *Electrochim. Acta*, 2015, **151**, 81-88.

[35] Y.M. Yeh, G.C. Tu and T.H. Fang, *J. Alloy. Compd* , 2004, **372** 224-230.

[36] G. Cacciamani, J. De Keyzer, R. Ferro, U.E. Klotz, J. Lacaze and P. Wollants, *Intermetallics*, 2006, **14**, 1312-1325.

[37] C.M. Fernandes and A.M.R. Senos, *Int. J. Refract. Met. Hard Mat.*, 2011, **29**, 405-418.

[38] X.Z. Jiang, S.A. Stevenson and J.A. Dumesic, *J. Catal.*, 1985, **91**, 11-24.

[39] X. Ding, Y. Liu, L. Gao and L. Guo, *J. Alloy. Compd.*, 2006, [illegible] 318-322.

[40] A. Atkinson, S. Barnett, R.J. Gorte, J.T.S. Irvine, A.J. McEvoy, M. Mogensen, S.C. Singhal and J. Vohs, *Nat. Mater.*, 2004, **3**, 17-27.

[41] E. Nikolla, J. Schwank and S. Linic, *J. Electrochem. Soc.*, 2009 **156**, B1312-B1316.